



Co-published by
Institute of Fluid-Flow Machinery
Polish Academy of Sciences
Committee on Thermodynamics and Combustion
Polish Academy of Sciences

Copyright©2024 by the Authors under licence CC BY 4.0.

<http://www.imp.gda.pl/archives-of-thermodynamics/>



Assessment of the impact of jet impingement technique on the energy efficiency of air-cooled BIPV/T roof tile

Jan Wajs^{a*}, Jakub Lukasik^a

^aFaculty of Mechanical Engineering and Ship Technology, Gdańsk University of Technology, Narutowicza 11/12, 80-233 Gdańsk, Poland

*jan.wajs@pg.edu.pl

Received: 19.11.2023; revised: 19.02.2024; accepted: 04.03.2024

Abstract

The paper concerns a numerical analysis of cooling of the hybrid photovoltaic (PV) modules dedicated to Building-Integrated Photovoltaic/Thermal (BIPV/T) systems. Attention was focused on the photovoltaic roof tiles, using a jet impingement technique, in which the intensification of heat transfer is ensured by streams of air hitting the heat exchange partition. A series of numerical simulations were carried out to assess an influence of the distance of the nozzle outlet from the absorber surface on the values of selected thermal-hydraulic performance indicators and the electrical parameters of the roof tile. The results confirmed the high effectiveness of the proposed method. The best effect was obtained for the case in which the relative distance of the nozzle from the partition to the nozzle diameter was equal to 1. For the mentioned configuration, an over 4 times increase in the value of the heat transfer coefficient was obtained in relation to the reference variant of cooling roof tiles. At the same time, the relative increase in the value of the generated electrical power was from 2.9 to 7.8%, depending on the value of the Reynolds number characterising the flow.

Keywords: Impinging jet; Building-Integrated Photovoltaic/Thermal (BIPV/T); Numerical analysis; Photovoltaic roof tile; Air cooling

Vol. 45(2024), No. 2, 5–18; doi: 10.24425/ather.2024.150847

Cite this manuscript as: Wajs, J., & Lukasik, J. (2024). Assessment of the impact of jet impingement technique on the energy efficiency of air-cooled BIPV/T roof tile. *Archives of Thermodynamics*, 45(2), 5–18.

1. Introduction

The photovoltaics sector is experiencing dynamic development, stimulated by the implementation of subsequent pro-ecological energy strategies. Investors expect an increase in energy efficiency while reducing costs and improving the aesthetics of the installation. In response, Building-Integrated Photovoltaic (BIPV) systems are becoming an interesting option and an increasingly developed branch of photovoltaics (PV). Due to the

limited possibility of natural cooling, they are operating under high temperature conditions, leading to a drop in generated power and a reduction in electrical efficiency. To improve the performance of various cooling systems, an effective management of the transferred heat is proposed. Such hybrid systems are known as Building-Integrated Photovoltaic/Thermal (BIPV/T). Air cooling is considered as one of the most promising and practical methods of cooling photovoltaic modules.

Nomenclature

a	– absorption coefficient, 1/m
D_h	– hydraulic diameter of the air duct at the inlet, m
D_j	– nozzle outlet diameter, m
D_{nb}	– nozzle base diameter, m
e	– specific energy, J/kg
\vec{g}	– vector of gravity acceleration, m/s ²
G	– distance of the nozzle outlet from the absorber plate, m
G_{sun}	– value of the solar irradiance at the front surface of the PV roof tile, W/m ²
h	– average heat transfer coefficient from the absorber surface, W/(m ² ·K)
H	– air duct height, m
H_j	– nozzle height, m
h_w	– heat transfer coefficient on the front surface of the module, W/(m ² ·K)
I	– radiation intensity, W/m ²
k_{eff}	– effective thermal conductivity coefficient including molecular and turbulent conductivity, W/(m·K)
L	– air duct length, m
\dot{m}	– air mass flow rate, kg/s
Ma	– Mach number
n_{ref}	– refractive index
Nu	– Nusselt number
δNu	– relative increase of Nusselt number compared to a straight channel collector
p	– pressure, Pa
Δp	– pressure loss, Pa
$\Delta P_{\%}$	– percentage increase in electrical power generation in relation to the reference variant, %
P_{mpp}	– temperature coefficient at the point of maximum power, %/K
P_{nom}	– nominal power, W
q	– heat flux, W/m ²
\vec{r}	– position vector
Re	– Reynolds number
s	– path length, m
\vec{s}	– direction vector, m
\vec{s}'	– scattering direction vector, m
S_1	– distance of the first transverse row of nozzles from the air duct inlet, m
S_2	– distance of the first longitudinal row of nozzles from the air duct edge, m
T	– local temperature, K
T_{abs}	– average temperature at the back wall of the absorber, K
T_b	– average air temperature between the inlet and outlet, K
ΔT_{cells}	– difference in average temperature of the silicon layer between the selected jet impingement variant and the reference variant, K
T_{cells}	– average temperature of the silicon layer in selected jet impingement variant, K

T_{cells_EVA}	– average temperature at the interface between silicon layer and EVA foil layer, K
T_{cells_ref}	– average temperature of the silicon layer in reference variant, K
T_{EVA_cells}	– average temperature at the interface between EVA foil layer and silicon layer, K
T_{out}	– average air temperature at the outlet of the flow duct, K
T_{surf}	– average surface temperature of the PV roof tile, K
\vec{v}	– velocity vector, m/s
V_{ch}	– channel inlet velocity, m/s
v_{in}	– average air velocity at the inlet to the flow duct, m/s
V_j	– nozzle outlet velocity, m/s
v_w	– wind speed, m/s
W	– air duct width, m
X	– distance between nozzles in the longitudinal direction, m
Y	– distance between nozzles in the transverse direction, m
y^+	– dimensionless wall distance

Greek symbols

α_p	– temperature coefficient at the point of max. power, %/K
η_{el_STC}	– electrical efficiency of the module in Standard Test Conditions (STC), %
η_{th}	– thermal efficiency, %
λ	– air thermal conductivity, W/(m·K)
$\mu _{t=25^\circ C}$	– dynamic viscosity coefficient of air at 25°C, kg/(m·s)
ρ	– fluid density, kg/m ³
$\rho _{t=25^\circ C}$	– air density at 25°C, kg/m ³
σ	– Stefan-Boltzmann constant, W/(m ² ·K ⁴)
σ_s	– scattering coefficient, 1/m
$\vec{\tau}$	– shear stress tensor, Pa
τ_{eff}	– total viscous stress tensor, Pa
Φ	– phase function
Ω	– solid angle, sr

Abbreviations and Acronyms

ASHRAE	– American Society of Heating, Refrigerating and Air-Conditioning Engineers
BIPV	– Building-Integrated Photovoltaic
BIPV/T	– Building-Integrated Photovoltaic/Thermal
DO	– Discrete Ordinates
EVA	– Ethylene-Vinyl Acetate
PEC	– Performance Evaluation Criteria
PV	– Photovoltaic
PVF	– Polyvinyl Fluoride
RANS	– Reynolds Averaged Navier-Stokes
RTE	– Radiative Transfer Equation
SAH	– Solar Air Heater
SST	– Shear Stress Transport
STC	– Standard Test Conditions
THPP	– Thermo-Hydraulic Performance Parameter

It has several advantages, such as unlimited availability, no cost of acquiring the medium, no negative impact on the environment, low system cost, and no problems with moisture, boiling, and freezing. On the other hand, the major disadvantage of this

system is a low value of the heat transfer coefficient. Therefore, effective methods of intensifying heat transport are being sought. In the authors' opinion, one of the most promising directions of improvement in this field is the application of the jet

impingement technique. The air stream hitting the absorber surface creates a thin layer with a high turbulence intensity near the point of impact, which, as a result of the high local values of the heat transfer coefficient, allows for effective heat removal.

There are publications available in the literature on the use of impinging jets to intensify the heat transfer from solar air heaters (SAH). One of the first works in this area was presented by Choundhury and Garg [1]. A perforated plate was a partition for generating the streams. The use of the jet impingement technique in the tested system allows for an increase in the temperature of the air leaving the duct by 15.5 K and an increase in the thermal efficiency of the system by 26.5%, compared to the system with airflow through a straight duct. Zukowski [2] proposed the construction of a microjet SAH, in which the air hitting the flat surface of the absorber plate ensures intensified heat removal. The experimental tests showed that the solar energy conversion efficiency using this solution ranged from 66% to 90%, which allows it to compete with the best solutions available on the market while being characterised by low pressure losses.

Current work on the use of jet impingement technology to remove heat from solar air heaters includes research on various geometric configurations of nozzles that direct the medium and their impact on the energy effects obtained. Chauhan et al. [3] examined the influence of the geometric parameters of the impinging jet system on the thermal efficiency and pressure losses of investigated SAH. The tests were carried out for a straight channel in the range of Reynolds number values from 3 800 to 16 000 determined at the inlet. The generation of air streams was ensured by a perforated plate placed halfway up the duct, at a distance of 25 mm from the absorber heat exchange surface. Attention was focused on the evaluation of geometric parameters in the form of the ratio of the longitudinal spacing of the holes to the duct hydraulic diameter (X/D_h), the ratio of transverse spacing to the duct hydraulic diameter (Y/D_h), as well as the ratio of the nozzle outlet diameter to the duct hydraulic diameter (D_j/D_h). The variant described by the parameters: $X/D_h = 0.435$, $Y/D_h = 0.869$, and $D_j/D_h = 0.065$ was considered as the optimal configuration with the Reynolds number equal to 16 000.

Yadav and Saini [4] using ANSYS 18.1 software conducted numerical studies on the impact of various configurations of dimensionless parameters describing the nozzle geometry on the efficiency of a solar air heater. The variables tested were the ratio of the nozzle height to the duct hydraulic diameter (H_j/D_h) and the ratio of the nozzle outlet diameter to the hydraulic diameter (D_j/D_h). The hydraulic diameter was specified at the inlet cross-section, and the lower part of flow duct was a straight channel with fixed dimensions. Simulations were performed at the Reynolds number range from 3 500 to 17 500. The results indicated that the recommended configuration that provided a favourable balance between the improvement of cooling efficiency and pressure drop was the ratio $H_j/D_h = 0.216$ and $D_j/D_h = 0.065$.

In the study conducted by Pazarlioglu et al. [5], the influence of various nozzle heights on the thermal efficiency of a SAH was assessed. The variable parameter in the tests was the dimensionless ratio of the distance of the nozzle outlet to the absorber plate to the constant diameter of the nozzle (G/D_j). The research

was carried out based on numerical analysis for the values of Reynolds numbers defined at the inlet in the range from 10 000 to 25 000. The best configuration for all the conditions tested at the inlet turned out to be the value of $G/D_j = 2$, which, despite generating the highest pressure drop values, achieved the highest value of the performance evaluation criteria (PEC) index.

Hai et al. [6] compared 7 configurations of parallel or crossing nozzles with different inclination angles. The thermo-hydraulic performance parameter (THPP) of the system was investigated for various geometric variables ($0.024 \leq D_j/D_h \leq 0.144$; $0.30 \leq X/D_h \leq 0.60$; $0.30 \leq Y/D_h \leq 0.60$), Reynolds numbers ($10\,000 \leq Re \leq 30\,000$), and the ratio of nozzle outlet velocity to the channel inlet velocity ($1 \leq V_j/V_{ch} \leq 25$). For low values of the V_j/V_{ch} ratio, higher THPP values were obtained for parallel configurations, while for high values, cross-shaped configurations performed better. It was also observed that the change in transverse and longitudinal nozzle spacing had no significant influence on the friction factor. In comparison with a smooth channel in conventional solar air heater, the best configuration caused an increase of the Nusselt number by up to 4.26 times.

Das et al. [7] presented a numerical parametric investigations on a SAH equipped with a perforated plate and conical protruded nozzles. The research focused on evaluating the influence of selected dimensionless parameters on the THPP indicator within a Reynolds number range from 2 900 to 14 300, defined at the channel inlet. Experimental validation of the results was also performed. The best configuration was found to be the variant described by the parameters $H_j/D_h = 0.2608$, $D_j/D_h = 0.0217$, and $D_{nb}/D_h = 0.0652$ (the ratio of nozzle base diameter to hydraulic diameter). For this configuration, at the maximum investigated Reynolds number, the Nusselt number value of 223.18 and a thermal efficiency of 91.25% were gained.

Ewe et al. [8] conducted numerical and experimental thermo-electro-hydraulic analysis of a jet impingement bifacial photovoltaic thermal collector. Configurations with different longitudinal ($0.09 \leq X \leq 0.126$ m) and transverse ($0.081 \leq Y \leq 0.1134$ m) jet hole spacings were investigated at two solar irradiance values (700 and 900 W/m²) and the Reynolds numbers ranging from 1 409 to 28 404. The system performance evaluation took into account a pressure drop and fan power required for flow circulation. The configuration with 36 jet holes reached the highest electrical energy output at a Reynolds number of 5 667, while the maximum thermal energy output was obtained at $Re = 9\,929$. The highest thermal, electrical, and thermo-electro-hydraulic efficiencies were equal to 57.3%, 10.36% and 83.93%, respectively.

Only a few studies in the literature refer to the use of a jet impingement technique for cooling PV modules, especially for removing heat from BIPV/T systems. A significant gap in this matter is confirmed by Ewe et al. [9]. The novelty of the presented paper is the presentation of the results of own work on the assessment of the impact of selected configurations of the cooling system with the jet impingement technique on the electrical and thermal-hydraulic parameters of the BIPV/T module in the form of a PV roof tile. The various nozzle length values, described in dimensionless form as the ratio of the nozzle outlet distance from the absorber surface to the nozzle diameter, were

taken into consideration. The approach proposed in this work is based on multivariant, numerical thermal-flow analyses. The simulations were carried out in the ANSYS Fluent software with the implemented Discrete Ordinates (DO) radiation model and the Solar Load module, allowing for a better representation of real atmospheric conditions. Analyses were carried out at a constant solar irradiance of $1\,000\text{ W/m}^2$ and the Reynolds numbers in the range of $5\,000$ – $25\,000$ for cooling airflow. The results were compared to the reference variant in which air flows freely through the channel and the rear wall of the absorber. The obtained distributions of temperature and velocity fields of the cooling medium were also visualised.

2. Scope of research and methodology

The research was carried out using the Monier Brass PV Premium roof tile model, with cells made of monocrystalline silicon. The technical parameters of investigated roof tile are listed in Table 1.

Table 1. Technical parameters of the tested photovoltaic roof tile [10].

Parameter	Value
Nominal power (P_{nom})	100 W
Electrical efficiency of the module in STC (η_{el_stc})	16.34%
Temperature coefficient of maximum power (P_{mpp})	$-0.42\%/K$
Module dimensions	$1\,825 \times 454\text{ mm}$
Dimensions of a single cell	$156 \times 156\text{ mm}$
Number of cells	22

To intensify heat transfer, 240 symmetrically arranged cylindrical nozzles were used, directing air streams to the module's absorber. The research focused on comparing the results obtained for variants with different nozzle lengths, marked as A, B, and C in Fig. 1, which visualises the tested flow systems with jet impingement technique. The selected configurations were described by the dimensionless parameter G/D_j , defined as the ratio of the distance of the nozzle outlet from the absorber surface (G) to the nozzle diameter (D_j). Variant C, described as $G/D_j = 12.61$, is a system with a perforated partition to generate streams (holes in the partition take over the function of the nozzles).

For reference purposes, the analyses of cooling under airflow conditions through a straight duct with a height of $H = 37.83\text{ mm}$ (variant D, where the aspect ratio $W/H = 12$) and a double-height duct, that is, $H = 75.66\text{ mm}$ (variant E, where $W/H = 6$) were carried out. The adopted aspect ratio values were obtained from the literature [7, 11, 12, 13] and refer to the ASHRAE 93–97 standard dedicated to solar air heaters [14]. The remaining geometric parameters, listed in Table 2, were taken from the literature [3, 5, 7] and were not optimised at the current stage of the investigation.

The Reynolds number values characterising the air flow were determined at the inlet to the duct using the equation:

$$Re = \frac{\rho|_{t=25^\circ C} \cdot v_{in} \cdot D_h}{\mu|_{t=25^\circ C}}, \quad (1)$$

where: $\rho|_{t=25^\circ C}$ – air density at $25^\circ C$ [kg/m^3]; v_{in} – average air velocity at the inlet [m/s]; D_h – hydraulic diameter of the air duct at the inlet [m]; $\mu|_{t=25^\circ C}$ – dynamic viscosity coefficient of air at $25^\circ C$ [$\text{kg/(m}\cdot\text{s)}$].

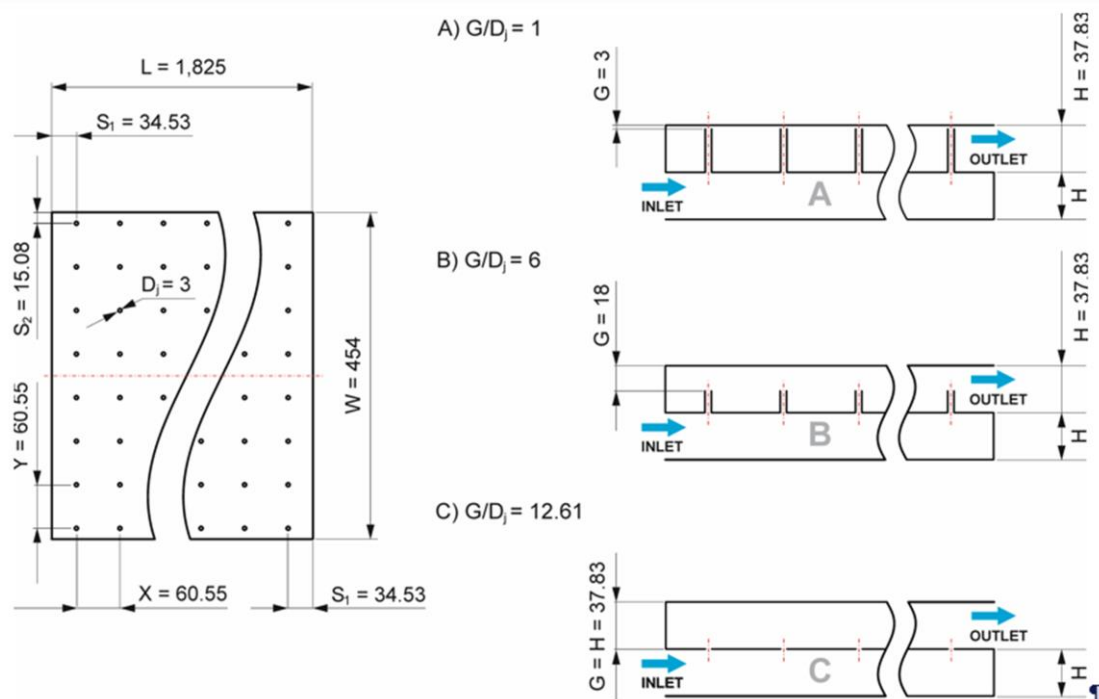


Fig. 1. Geometry of considered airflow ducts with jet impingement technique (variants A, B, C represent various nozzle lengths).

Table 2. Geometric parameters of the tested configurations.

	Variants A, B, C	Variant D	Variant E
Height of the airflow duct (H , mm)	37.83	37.83	75.66
Hydraulic diameter (D_h , m)	0.07	0.07	0.13
Air duct aspect ratio (W/H)	12	12	6
Nozzle diameter (D_j , mm)	3	n/a	n/a
Nozzle diameter to hydraulic diameter ratio (D_j/D_h)	0.043	n/a	n/a
Nozzle spacing in the longitudinal direction (X/D_h)	0.867	n/a	n/a
Nozzle spacing in the transverse direction (Y/D_h)	0.867	n/a	n/a

The values of Reynolds numbers analysed in each configuration, defined at the inlet to the airflow duct, correspond to the values of mass flow rates listed in Table 3.

Table 3. Mass flow rate values corresponding to the analysed Reynolds number values.

Re [-]	\dot{m} [kg/s]	
	Variant A, B, C, D ($H = 37.83$ mm)	Variant E ($H = 75.66$ mm)
5000	0.0226	0.0243
10000	0.0451	0.0486
15000	0.0678	0.0729
20000	0.0903	0.0971
25000	0.1128	0.1215

The heat transfer coefficient at the front surface of the module was determined according to the correlation proposed in [15]:

$$h_w = 5.7 + 3.8 \cdot v_w, \quad (2)$$

where: v_w is the wind speed [m/s]. An extreme theoretical case was assumed in which the wind speed is 0 m/s.

The average coefficient of heat transfer at the absorber surface was determined from the relationship:

$$h = \frac{q}{T_{abs} - T_b}, \quad (3)$$

where: q – transferred heat flux [W/m^2]; T_{abs} – average temperature at the back wall of the absorber [K]; T_b – average air temperature between the duct inlet and outlet [K].

The Nusselt number was defined as:

$$Nu = \frac{h \cdot D_h}{\lambda}, \quad (4)$$

where: λ is the air thermal conductivity [$W/(m \cdot K)$].

The thermal efficiency of the individual variants was determined from the formula:

$$\eta_{th} = \frac{q}{G_{sun}}, \quad (5)$$

where: G_{sun} – value of the solar irradiance at the front surface of the PV roof tile ($1000 W/m^2$).

To consider the improvement of the power generation of the photovoltaic roof tile, its structure has to be taken into account. The cross-section of the photovoltaic roof tile is presented in Fig. 2, including the thicknesses of each layer and the key temperatures marked.

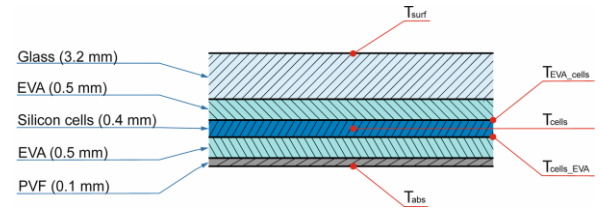


Fig. 2. Modelled layers of photovoltaic roof tile [17].

The estimation of an increase in the electrical power generation in the variants with jet impingement technique (A–C), compared to the reference variant with a straight channel (D), was described by the formula:

$$\Delta P_{\%} = \alpha_p \cdot \Delta T_{cells}, \quad (6)$$

where: α_p – temperature coefficient at the point of maximum power [%/K], ΔT_{cells} – difference in average temperature of the silicon layer between the selected jet impingement variant and the reference variant [K].

To determine ΔT_{cells} , the temperature of silicon layer for each variant with jet impingement technique (A–C) as well as the reference variant (D) must be known:

$$\Delta T_{cells} = T_{cells} - T_{cells_ref}, \quad (7)$$

where: T_{cells} – average temperature of the silicon layer in selected jet impingement variant [K]; T_{cells_ref} – average temperature of the silicon layer in reference variant [K].

The average temperature of the silicon layer was determined as the arithmetic one between the averaged temperature at the interface of the EVA foil layer - silicon layer and silicon layer - EVA foil layer. It was calculated using the formula:

$$T_{cells} = \frac{T_{EVA_cells} + T_{cells_EVA}}{2}, \quad (8)$$

where: T_{EVA_cells} – average temperature at the interface between EVA foil layer and silicon layer [K]; T_{cells_EVA} – average temperature at the interface between silicon layer and EVA foil layer [K].

The above temperature values for each individual layers of the PV module were obtained numerically as the averages over total layer surface.

Taking the temperature of the silicon layer as an average in calculation of electrical power increase was a simplification introduced to determine the overall effect. This assumption was necessary because the local temperature distribution in particular cells was variable as a result of cooling. It leads to different voltage-current operating points. Therefore, to evaluate the operation of the entire module, the averaging procedure was conducted.

Numerical calculations were performed using ANSYS Fluent 2021 R1 software. Constant values of the thermophysical properties of the materials used, taken from the literature, were assumed for the calculations. They are summarised in Table 4.

All layers of the photovoltaic module except the protective glass were modelled using a 2D shell conduction approach. The glass layer, as a semi-transparent material, was modelled using a classic 3D approach. A conformal polyhedral mesh was used. To maintain satisfactory values of the quality of the skewness and orthogonality coefficient, the mesh size was locally refined. For variant A ($G/D_j = 1$) and variant D ($H = 37.83$ mm), at the $Re = 25\,000$, a mesh independence test was performed. In variant A, meshes with a number of cells ranging from 2.25 million to 6.65 million were tested, with steps of approximately 0.7 million, and in variant D from 0.18 million to 1.28 million, in steps of approximately 0.18 million. The condition ending the tests was the conjunction of events, defined as a relative difference of the Nusselt number value between the previous and current results less than 1% and a relative difference of the heat flux transferred by the air between the previous and current results less than 1%. Table 5 presents the results of the mesh sensitivity analysis.

Ultimately, the adapted meshes, ensuring a compromise between the accuracy of the results and the calculation time, consisted of approximately 5.47 million cells. The coefficient

$y^+ = 0.991$ averaged for all analysed Reynolds number values for variant A, and approximately 1.08 million cells, with the coefficient $y^+ = 0.847$ for variant D was obtained. Ten levels within the boundary layer were created using a constant growth rate of 1.3. The visualisation of the mesh prepared for variant A is presented in Fig. 3.

The finite-volume method for 3D geometry was used to solve the thermal-flow model. Due to the low velocity value ($Ma < 0.2$), the flow was treated as incompressible. A pressure-based solver, the Reynolds Averaged Navier-Stokes (RANS) equations, and the shear stress transport (SST) $k-\omega$ turbulence model suggested by Hussein et al. [23] and Tepe et al. [24] were used. Stationary simulations were performed, without internal sources of heat and mass. The boundary conditions at the inlet were set in the form of a constant value of the mass flow rate to maintain the individual values of the Reynolds numbers and a constant inlet air temperature of 25°C. A fully developed velocity profile prepared using a translational periodic interface was used. The pressure at the outlet from the flow duct was assumed to be equal to atmospheric pressure. The equations of continuity, momentum, and energy have the following form [23, 25, 26]:

Continuity equation:

$$\nabla \cdot \vec{v} = 0, \quad (9)$$

where: \vec{v} – velocity vector [m/s].

Table 4. Thermophysical properties of the materials used [16–22].

Material	Density [kg/m ³]	Specific heat [J/(kg·K)]	Thermal conductivity [W/(m·K)]	Refractive index [–]	Emissivity [–]
Air (at 25°C)	1.185	1 005	0.0263	1	–
Glass	3 000	500	1.8	1.5	0.94
EVA foil	960	2 090	0.35	1.5	0.94
Silicon cells	2 330	677	148	–	0.9
PVF	1 200	1 250	0.2	–	0.98

Table 5. Results of the mesh independence test for the case with $Re = 25\,000$.

	Mesh No.	Number of cells	y^+	Nu	$\delta Nu\%$	q [W/m ²]	$\delta q\%$
Variant A ($G/D_j = 1$)	Mesh 1	2 252 793	7.283	651.45	–	740.86	–
	Mesh 2	3 298 981	4.125	443.35	–31.94%	739.61	–0.17%
	Mesh 3	3 889 612	3.046	391.14	–11.78%	739.41	–0.03%
	Mesh 4	4 454 470	2.316	371.86	–4.93%	740.78	0.15%
	Mesh 5	4 955 807	2.276	367.50	–1.17%	740.39	–0.05%
	Mesh 6	5 472 638	2.232	364.64	–0.78%	740.11	–0.04%
	Mesh 7	6 646 577	2.186	361.91	–0.75%	740.02	–0.01%
Variant D ($H = 37.83$ mm)	Mesh 1	180 813	7.912	111.33	–	602.46	–
	Mesh 2	371 959	2.662	103.85	–6.72%	625.57	3.69%
	Mesh 3	489 004	2.182	97.56	–6.06%	619.86	–0.92%
	Mesh 4	601 102	1.924	95.33	–2.29%	618.38	–0.24%
	Mesh 5	877 811	1.576	94.14	–1.25%	619.29	–0.15%
	Mesh 6	1 078 662	1.428	93.75	–0.41%	619.90	–0.10%
	Mesh 7	1 283 286	1.377	93.51	–0.25%	620.05	0.02%

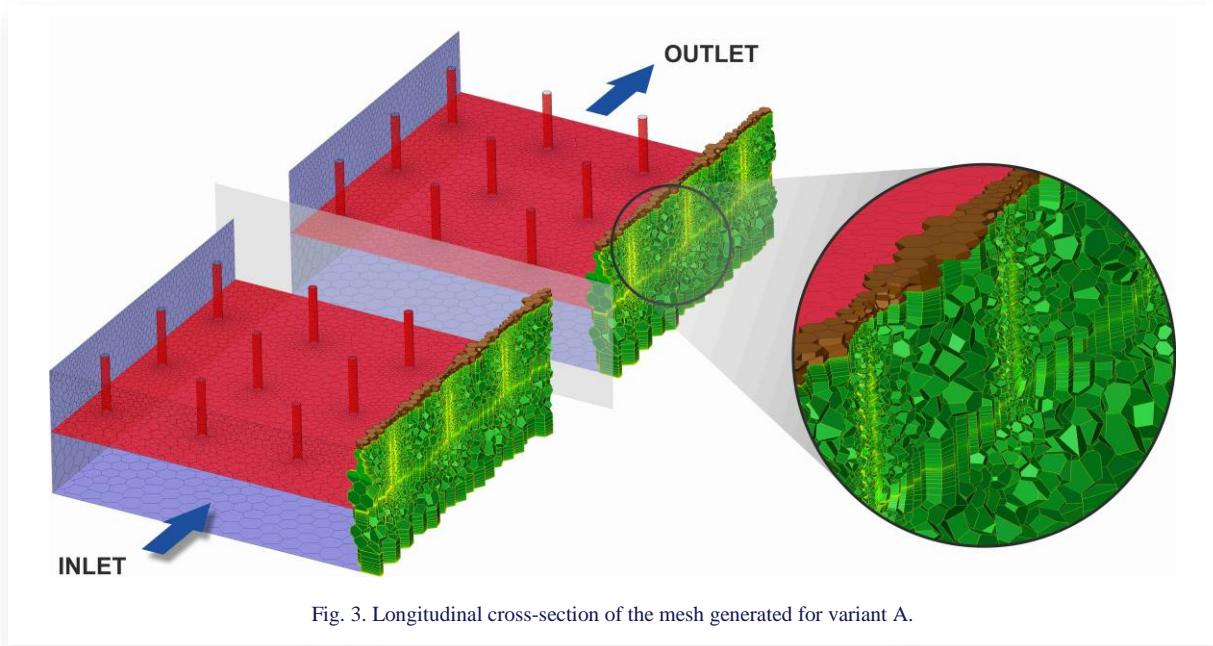


Fig. 3. Longitudinal cross-section of the mesh generated for variant A.

Momentum conservation equation:

$$\nabla \cdot (\rho \vec{v} \vec{v}) = -\nabla p + \nabla \cdot \vec{\tau} + \rho \vec{g}, \quad (10)$$

where: ρ – fluid density [kg/m³]; p – pressure [Pa]; $\vec{\tau}$ – shear stress tensor [Pa]; \vec{g} – vector of gravity acceleration [m/s²].

Energy conservation equation:

$$\nabla \cdot (\vec{v}(\rho e + p)) = \nabla \cdot (k_{eff} \nabla T + \vec{\tau}_{eff} \cdot \vec{v}), \quad (11)$$

where: e – specific energy [J/kg]; k_{eff} – effective thermal conductivity coefficient including molecular and turbulent conductivity [W/(m·K)]; T – local temperature [K]; $\vec{\tau}_{eff}$ – total viscous stress tensor [Pa].

All external walls of the system, except the front surface of the module, were considered adiabatic. The partition between the upper and lower part of the duct was also considered adiabatic. The internal walls at the boundary between the solid and fluid domains were treated as no-slip walls [27]. To reflect the solar radiation falling at the front surface of the module, the Discrete Ordinates radiation model was used, enabling modelling of semi-transparent domains. The Solar Load extension has also been implemented. Radiation modelling is based on the radiative transfer equation (RTE), which determines the intensity of radiation transported from position \vec{r} towards direction \vec{s} . In accordance with literature [25,26,28], radiation intensity (I [W/m²]) is defined using equation (12), where: \vec{r} – position vector [m]; \vec{s} – direction vector [m]; s – path length [m]; a – absorption coefficient [1/m]; σ_s – scattering coefficient [1/m]; n_{ref} – refractive index [–]; σ – Stefan-Boltzmann constant [W/(m²·K⁴)]; \vec{s}' – scattering direction vector; Φ – phase function [–]; Ω – solid angle [sr].

It was assumed that the radiation falls on the front surface of the PV roof tile in the normal direction and there is no reflected radiation. A constant solar irradiance equal to 1 000 W/m² was assumed. The calculations used a coupled solver and double precision of numerical notation. Due to the satisfactory values of aspect ratio, orthogonal quality, and skewness, the second-order upwind discretisation scheme was used.

3. Results and discussion

The obtained values of thermal-hydraulic performance indicators were presented as graphs plotted as a function of the Reynolds number. Figure 4 (a) shows the profiles of the average air temperature at the outlet of the flow duct (T_{out}) and the received heat flux (q). Figure 4 (b) presents the profiles of the average temperature at the module front surface (T_{surf}) and the average heat transfer coefficient from the absorber surface (h). Figure 5 (a) shows the profiles of the Nusselt number (Nu) and the thermal efficiency values of the photovoltaic roof tile (η_{th}). Figure 5 (b) presents the characteristics of pressure drops in the flow channel (Δp) and the absolute temperature difference of the module in the silicon cells layer (ΔT_{cells}) between the variants with the jet impingement technique (A, B, C) and the reference variant (D).

In terms of thermal performance, the best results in the entire range of tested Reynolds number values were achieved for variant A with the outlet of the nozzle placed the closest to the absorber ($G/D_j = 1$). Compared to the reference variant with a straight channel (D) and a height of $H = 37.83$ mm, the temperature of the air leaving the flow duct increased by 5.7 K, 1.3 K, and 0.6 K at Reynolds numbers of 5 000, 15 000 and 25 000, respectively.

$$\frac{dI(\vec{r}, \vec{s})}{ds} = -(a + \sigma_s)I(\vec{r}, \vec{s}) + a \frac{n_{ref}^2 \sigma T^4}{\pi} + \frac{\sigma_s}{4\pi} \int_0^{4\pi} I(\vec{r}, \vec{s}') \Phi(\vec{s} \cdot \vec{s}') d\Omega' \quad (12)$$

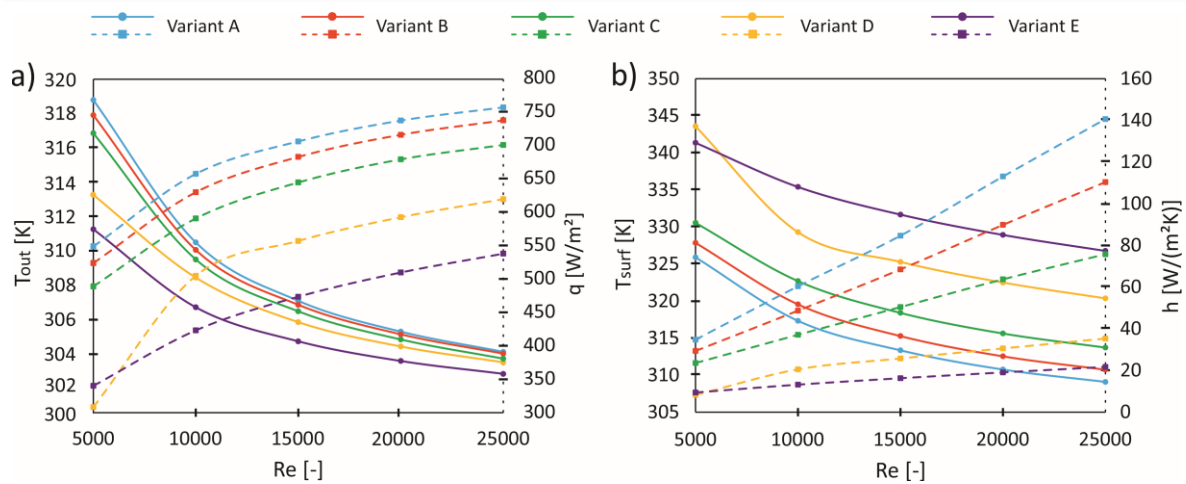


Fig. 4. Characteristics of: (a) average air temperature at the outlet and heat flux transferred by the air; (b) average temperature at the front surface of the module and average heat transfer coefficient at the absorber surface.

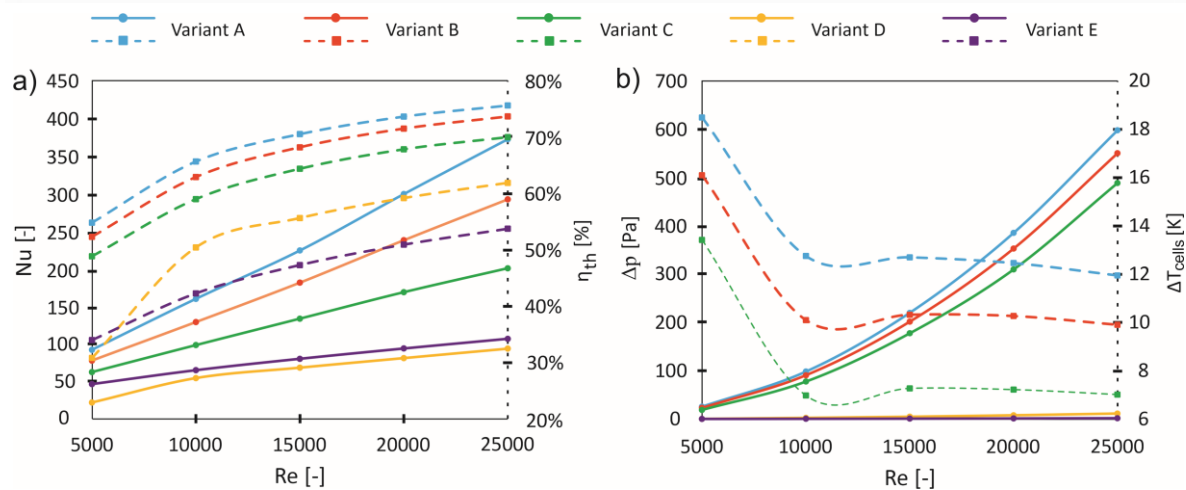


Fig. 5. (a) Profiles of the Nusselt number and thermal efficiency values of the photovoltaic roof tile; (b) Characteristics of pressure drops in the flow channel and the module temperature difference in the silicon layer between the variants with the jet impingement technique and the reference variant.

The temperature drops at the front surface module were 17.7 K, 11.9 K, and 11.3 K, respectively. Heat flux increased by 240.9 W/m² (78.1%), 149.22 W/m² (26.8%), and 137.6 W/m² (22.2%). The value of the heat transfer coefficient increased by 26.5 W/(m²·K), 58.9 W/(m²·K), and 105.3 W/(m²·K), and the Nusselt number by 70.4 (320.7%), 156.4 (228.5%) and 279.6 (298.1%).

In the case of variant C, with a perforated plate without nozzles, the temperature of the air leaving the system increased by 3.7 K, 0.7 K, and 0.2 K, while the temperature drop on the surface was reduced by 13.0 K, 6.9 K, and 6.6 K at Reynolds numbers of 5 000, 15 000, and 25 000, respectively. The heat flux increased by 181.0 W/m² (58.7%), 87.6 W/m² (15.7%), and 81.3 W/m² (13.1%). The heat transfer coefficient increased by 15.3 W/(m²·K), 24.6 W/(m²·K), and 40.4 W/(m²·K), and the Nusselt number increased by 40.6 (185.1%), 65.4 (95.6%) and 107.4 (114.5%). Intermediate points for Re = 10 000 and

Re = 20 000 are also presented in the graphs shown in Figs. 4 and 5 for each configuration.

The results indicate that the differences in the temperature of the air leaving the flow channel, the heat flux transferred by the air, and the temperature at the front surface of the module between the leading variant A and the reference variant D decrease with an increase in the Reynolds number. The largest differences occur for the configuration with the lowest considered Reynolds number. Significantly smaller differences are observed between configurations with Reynolds number in the range of 10 000–25 000. This allows to assume that in practical applications, in the thermal aspect related to the potential use of heated air, taking into account the energy required to force the flow and overcome hydraulic resistance, increasing the velocity of the air above a certain limit may not be justified. A significant increase in hydraulic resistance is noticeable, which for variant A, compared to the reference variant D, resulted in an increase in the pressure drop in the flow channel by 28.8 Pa (79 times), 245.9 Pa (46

times), and 670.3 Pa (53 times), at the Reynolds number values of 5 000, 15 000 and 25 000 respectively. The thermal efficiency values for variants A and D presented in the analogous Reynolds number convention were 54.9%, 70.7%, and 75.8% for variant A and 30.8%, 55.8%, and 62.0% for variant D.

Table 6 shows the estimated increase in electrical power generated by the PV roof tile compared to the reference variant (D).

Table 6. Estimated increase in generated electrical power compared to the reference variant (D).

Re [–]	Variant A	Variant B	Variant C
5 000	7.77%	6.76%	5.64%
10 000	5.36%	4.24%	2.93%
15 000	5.33%	4.33%	3.05%
20 000	5.22%	4.31%	3.03%
25 000	5.02%	4.16%	2.95%

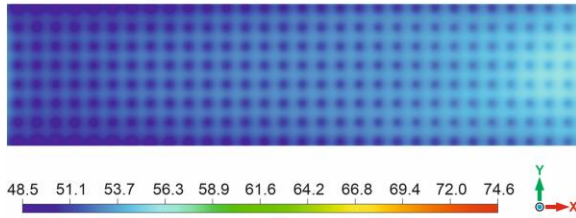
The results obtained indicate a significant increase in the electrical power generated by the PV roof tile, in relation to the configuration with straight cooling channel (variant D). The highest increase in a power is characterised by variant A, which allows to increase the power supply to the system by approximately 7.8%, 5.3%, and 5.0% at the Reynolds number values of 5 000, 15 000, and 25 000, respectively. The variant with an intermediate nozzle length (B) and the variant with a perforated partition generating the streams (C) reached an increase approximately

1% and 2% lower, respectively, compared to the leading variant (A).

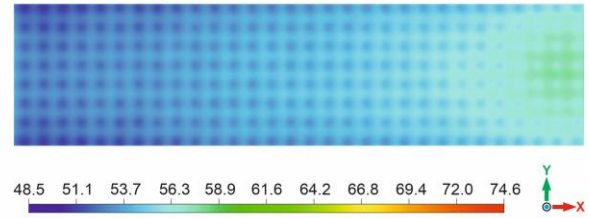
The differences in the estimated electrical power generated in variants A–C result from the temperature of the silicon cell layer, achieved by varying the distance between the nozzle outlet and the lower surface of the absorber. Similar to the module surface temperature, the silicon cell layer temperature is the lowest in variant A. This translates to the highest potential for increasing the generated power compared to the reference variant with a straight channel (D). In each configuration with jet impingement, it is also observed that the relative increase in generated power decreases with increasing Reynolds number, particularly in the Reynolds number range of 10 000–25 000. This is due to the diminishing difference between the average silicon cell layer temperature in the different jet impingement variants and the average cell layer temperature in the reference variant D, as the Reynolds number increases. As a result, the increase in Reynolds number has a progressively smaller impact on the relative increase in electrical power of the photovoltaic roof tile compared to the straight channel variant. This provides a field for future system optimisation based on the adopted objective function.

Figures 6–10 present local distributions of selected thermal-hydraulic parameters for the analysed variants. Figures 6 and 7 show the temperature distributions at the front surface of the

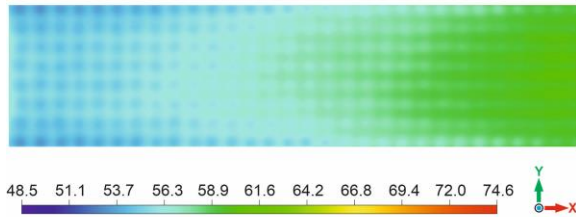
Variant A ($G/D_j = 1$); $Re = 5\,000$



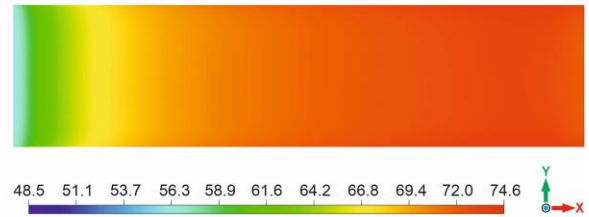
Variant B ($G/D_j = 6$); $Re = 5\,000$



Variant C ($G/D_j = 12.61$); $Re = 5\,000$



Variant D ($H = 37.83\text{ mm}$); $Re = 5\,000$



Variant E ($H = 75.66\text{ mm}$); $Re = 5\,000$

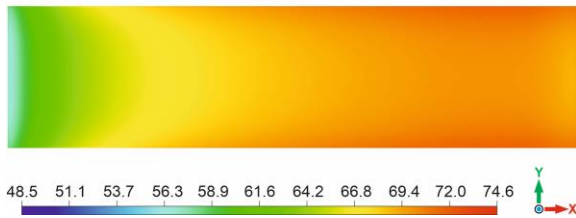
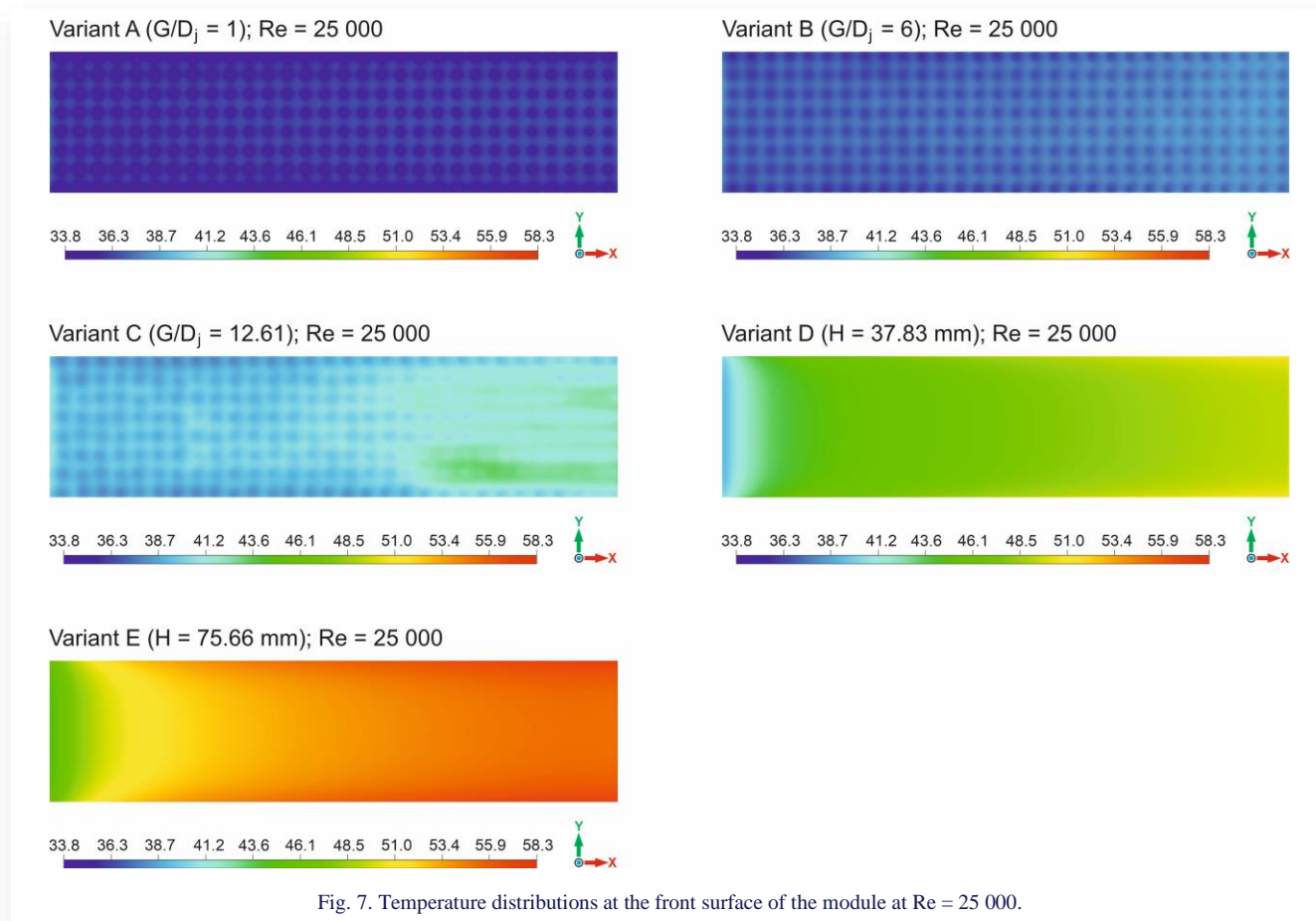


Fig. 6. Temperature distributions at the front surface of the module at $Re = 5\,000$.



module for the flow characterised by the limiting tested Reynolds number of 5 000 and 25 000, respectively for all configurations of flow duct. The graphics presented in Figures 8–10 exhibit the longitudinal cross-section (xz) of a PV roof tile. They include 5 rows of nozzles located in the centre of the flow channel (lateral rows 13–17). The cross-section with the xz plane represents the 4th longitudinal row. Figure 8 shows the local temperature distribution, while Figure 9 shows the local velocity distribution, and Figure 10 presents the vector velocity field (x and z components). For graphics referring to the same value of the Reynolds number, a uniform colour scale is used to facilitate the capture of differences between individual configurations.

The temperature distribution at the front surface of the photovoltaic roof tile shows a change in the temperature field directed from the inlet to the outlet, along the x -axis, towards higher values. It is a result of the combined effects of the gradual heating of the air flowing along the absorber through the channel towards the outlet and, in the case of variants with the jet impingement technique, mixing of cold air supplied from the lower part of the duct with the heated air in the upper part. The effect of a local increase in the heat transfer coefficient, manifested by a lower temperature in the area affected by the air flowing from the nozzles, is smaller when the nozzle outlet is located farther from the absorber surface.

For the longitudinal cross-section presented (Fig. 8) in the area from the 13th to the 17th row of nozzles, there is a uniform temperature distribution in each nozzle, resulting from the assumption of adiabaticity of the partition separating the channels and adiabaticity of the nozzles themselves. At the same time,

much lower temperature values are observed in the upper part of the flow duct for the configuration with higher Reynolds number values. Moreover, for the variant C with a perforated partition and $Re = 5\,000$ a rapid heating of the air flowing from the holes is visible. Near the absorber, the air discharged from the holes reached a temperature close to the average air temperature in the upper part of flow duct considered in a given cross-section. This is due to the low velocity at which the air moves out the holes, which quickly mixes and exchanges heat with the air transported in the upper channel. A general deviation of the air stream leaving the holes in the perforated partition toward the outlet is observed, as illustrated in Fig. 9.

Figure 10 presents the velocity vector fields taking into account the x and z components. The deviation of the vectors in the area of air impact on the module absorber presents the air vortices occurring near the nozzle outlet. In the upper part of the duct, a vector velocity field was directed towards the outlet. In the lower part of duct, a velocity profile developed from the lower wall of the flow channel towards the flow core, and air rotation occurring in the area of air attack at the lower edges of the nozzles is observed.

The obtained results were compared with the achievements reported in the literature concerning the application of jet impingement technique in solar systems. According to the authors' best knowledge, publications specifically dedicated to air-based jet impingement adopted to PV/T and BIPV/T systems are very limited. Therefore, reference was also made to studies regarding solar air heaters. Table 7 presents a comparison of the authors' results, with those reported in the literature.

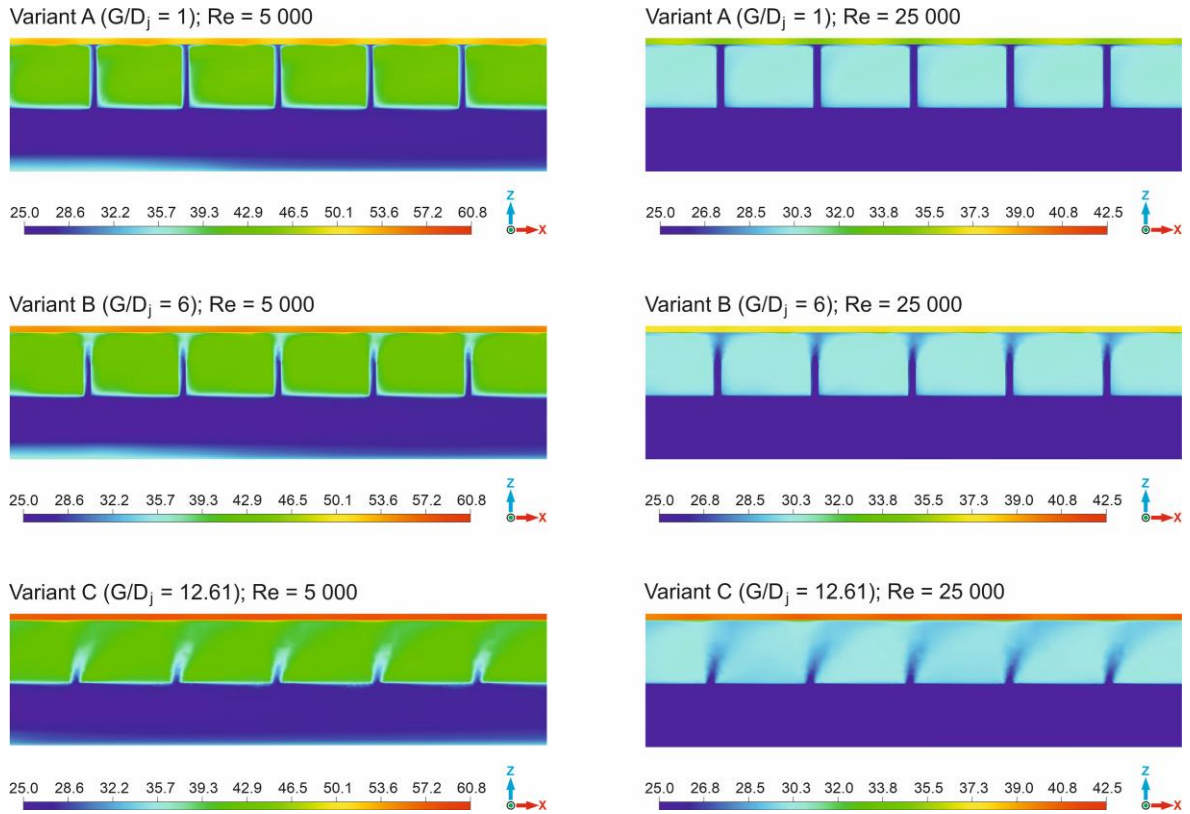


Fig. 8. Temperature distributions in the longitudinal cross-section for variants with the jet impingement technique.

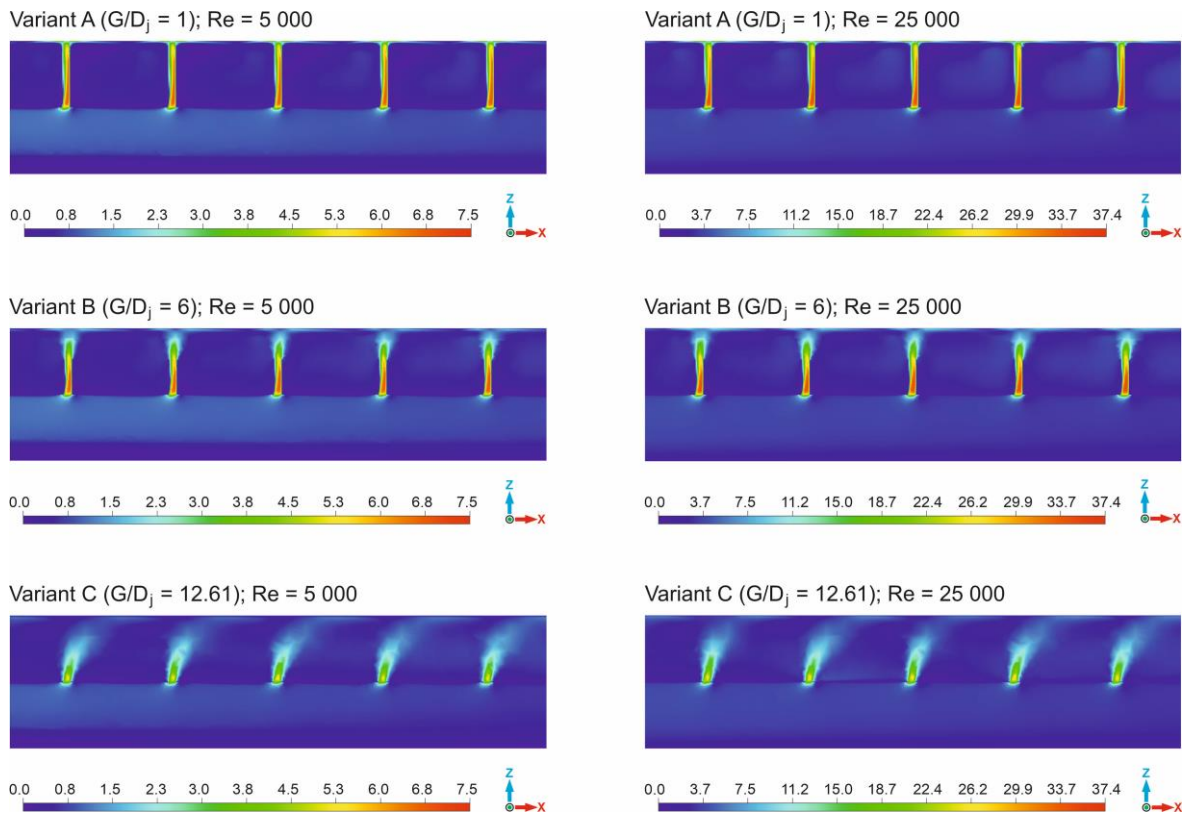


Fig. 9. Velocity distributions in the longitudinal cross-section for variants with the jet impingement technique.

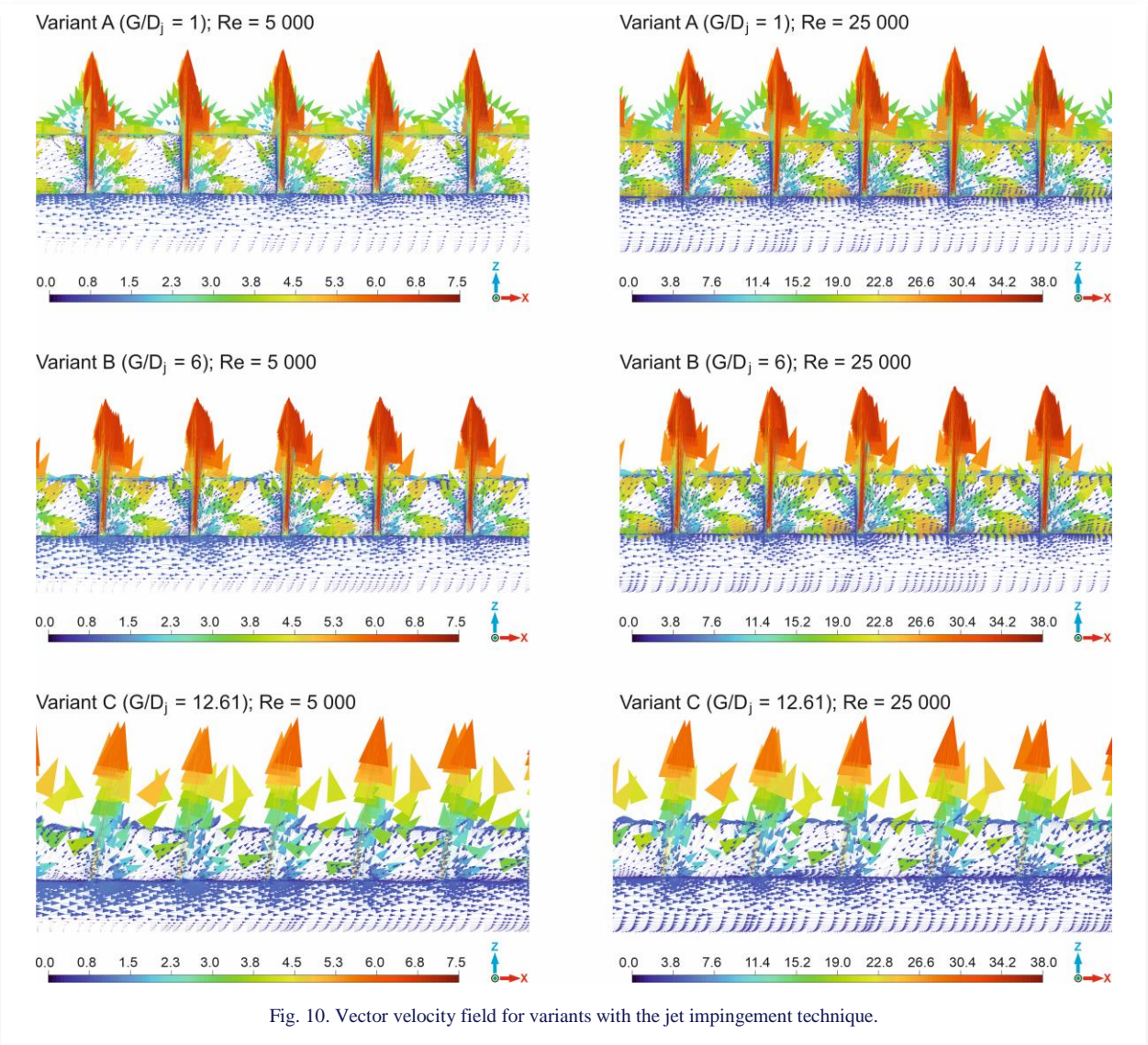


Fig. 10. Vector velocity field for variants with the jet impingement technique.

Table 7. Comparison with previous studies.

Reference / Year	Type of study		Re [–]	Nu [–] (δNu [%])	Thermal efficiency [%]	Remarks
	Exp.	Num.				
Present study	–	+	5 000–25 000	62.6–373.4 (80.8–320.7)	48.9–75.8	BIPV/T collector with elongated nozzles
[6] / 2023	–	+	10 000–30 000	(117–426)	–	SAH with inclined nozzles
[7] / 2023	+	+	2 900–14 300	135–223.2 (202.4–400.0)	42–91	SAH with conical protruded nozzles
[8] / 2022	+	+	1 409–28 404	–	36.5–65.0	Bifacial PV/T with jet plate
[5] / 2022	–	+	10 000–25 000	78.5–232.1	65.4–74.9	SAH with elongated nozzles
[4] / 2020	–	+	3 500–17 500	44–355 (454–758)	–	SAH with elongated nozzles

In Table 7 only values associated with jet impingement configurations were considered. In the Nusselt number column, relative increase compared to a straight channel collector with the same inlet dimensions and similar input parameters is given in parentheses. Validation of the results obtained in this study confirms that the application of jet impingement technique is an effective and promising solution for enhancing heat transfer in solar systems. The own research results are fully reflected in the

achievements presented in the literature. However, it should be noted that the studies presented in the literature are of a numerical or experimental nature, involving different geometric configurations and varied input parameter configurations. Therefore, direct comparison of values obtained by different authors and drawing general conclusions without individual analysis of specific cases is not recommended.

4. Conclusions

At the current stage of research, a numerical thermal-flow model of the proposed photovoltaic roof tile cooling system, based on the jet impingement technique, has been developed to fill the gap existing in the literature. The simulations performed confirm the high efficiency of heat transfer intensification using air streams hitting the module absorber. The following are the study's key findings:

- I. In terms of thermal performance, the best results in the entire range of tested Reynolds numbers were achieved for variant A with the outlet of the nozzle closest to the absorber ($G/D_j = 1$).
- II. The thermal benefits obtained vary in terms of the input conditions, characterised by the Reynolds number defined at the inlet to the flow channel. In each case, the results significantly exceeded the parameters obtained for the reference variant D, with the flow carried out through a straight duct with a height of $H = 37.83$ mm.
- III. At the $Re = 5\,000$, a decrease in the average temperature on the module surface by 17.7 K and an increase in the average air temperature at the outlet of the flow channel by 5.7 K were achieved. The value of the heat flux increased by 78.1%, and the relative increase in the value of the heat transfer coefficient and Nusselt number was 320.7%. The thermal efficiency of the system increased by 24.1%.
- IV. In the case of higher values of the analysed Reynolds numbers, the relative increases, in relation to the reference variant D, were not so high, but the absolute values of the thermal parameters reached even more favourable values.
- V. At all analysed values of the Reynolds number, the pressure drop in the airflow channel was several dozen times higher than for the reference variant D, drawing attention to the importance of the issue of hydraulic resistance occurring as a result of used technique.
- VI. The estimated electrical benefits showed that by using the jet impingement technique, depending on the Reynolds number and the configuration of the dimensionless parameter G/D_j , it is possible to obtain an increase in the generated electrical power in the range from 2.9% to 7.8% in relation to the reference variant.

In the next steps, it is planned to compare the results obtained for different nozzle shapes and optimize the geometric parameters of the photovoltaic roof tile cooling system based on the jet impingement technique, focused on maximising energy benefits in practical applications

Acknowledgements

The authors extend their appreciation to Krzysztof Abucewicz for his support with the preparation of drawings.

References

[1] Choudhury, C., & Garg, H.P. (1991). Evaluation of a jet plate solar air heater. *Solar Energy*, 46, 199-209. doi: 10.1016/0038-092X(91)90064-4.

[2] Zukowski, M. (2015). Experimental investigations of thermal and flow characteristics of a novel microjet air solar heater. *Applied Energy*, 142, 10-20. doi: 10.1016/j.apenergy.2014.12.052.

[3] Chauhan, R., Singh, T., Thakur, N.S., & Patnaik, A. (2016). Optimization of parameters in solar thermal collector provided with impinging air jets based upon preference selection index method. *Renewable Energy*, 99, 118-126. doi: 10.1016/j.renene.2016.06.046.

[4] Yadav, S., & Saini, R.P. (2020). Numerical investigation on the performance of a solar air heater using jet impingement with absorber plate. *Solar Energy*, 208, 236-248. doi: 10.1016/j.solener.2020.07.088.

[5] Pazarlıoğlu, H.K., Tepe, A.Ü., Tekir, M., & Arslan, K. (2022). Effect of new design of elongated jet hole on thermal efficiency of solar air heater. *Therm. Sci. Eng. Prog.*, 36, 101483. doi: 10.1016/j.tsep.2022.101483.

[6] Hai, T., B Mansir, I., Alshuraiaan, B., M Abed, A., Elhosiny Ali, H., Dahari M., & Albalawi H. (2023). Numerical investigation on the performance of a solar air heater using inclined impinging jets on absorber plate with parallel and crossing orientation of nozzles. *Case Studies in Thermal Engineering*, 45, 102913. doi: 10.1016/j.csite.2023.102913.

[7] Das, S., Biswas, A., & Das, B. (2023). Parametric investigation on the thermo-hydraulic performance of a novel solar air heater design with conical protruded nozzle jet impingement. *Applied Thermal Engineering*, 219, Part B, 119583. doi: 10.1016/j.applthermaleng.2022.119583.

[8] Ewe, W.E., Fudholi, A., Sopian, K., Moshery, R., Asim, N., Nuriyana, W., & Ibrahim, A. (2022). Thermo-electro-hydraulic analysis of jet impingement bifacial photovoltaic thermal (JIBPVT) solar air collector. *Energy*, 254, Part B, 124366. doi: 10.1016/j.energy.2022.124366.

[9] Ewe, W.E., Fudholi, A., & Sopian, K.B. (2022). Jet impingement cooling applications in solar energy technologies: Systematic literature review. *Thermal Science and Engineering Progress*, 34, 101445. doi: 10.1016/j.tsep.2022.101445.

[10] BMI Brass – Photovoltaic Systems brochure, <https://www.monier.pl/produkty/systemy-fotowoltaiczne/energia-el-ektryczna/braas-pv-premium.html> [accessed 16 Oct. 2023].

[11] Maithani, R., Sharma, S., & Kumar, A. (2021). Thermo-hydraulic and exergy analysis of inclined impinging jets on absorber plate of solar air heater. *Renewable Energy*, 179, 84-95. doi: 10.1016/j.renene.2021.07.013.

[12] Nadda, R., Kumar, A., & Maithani, R. (2017). Developing heat transfer and friction loss in an impingement jets solar air heater with multiple arc protrusion obstacles. *Solar Energy*, 158, 117-131. doi: 10.1016/j.solener.2017.09.042.

[13] Chauhan, R., Thakur, N.S., Singh, T., & Sethi, M. (2018). Exergy based modeling and optimization of solar thermal collector provided with impinging air jets. *Journal of King Saud University - Engineering Sciences*, 30, 355-362. doi: 10.1016/j.jksues.2016.07.003.

[14] ASHRAE Standards Committee. (1997). *Methods of testing to determine the thermal performance of solar collectors*. <https://www.ashrae.org/>.

[15] McAdams, W.H. (1954). *Heat transmission*, 3rd Edn. McGraw-Hill, Tokyo, Japan.

[16] Engineering ToolBox (2001). <https://www.engineeringtoolbox.com> [accessed 06 Apr. 2023].

[17] Hernandez-Perez, J.G., Carrillo, J.G., Bassam, A., Flota-Banuelos, M., & Patino-Lopez, L.D. (2021). Thermal performance of a discontinuous finned heatsink profile for PV passive cooling. *Applied Thermal Engineering*, 184, 116238. doi: 10.1016/j.applthermaleng.2020.116238.

[18] Leow, W.Z., Irwan, Y.M., Safwati, I., Irwanto, M., Amelia, A.R., Zhubir, N.S., Fahmi, M.I., & Rosle, N. (2020). Simulation study on photovoltaic panel temperature under different solar radiation using computational fluid dynamic method. *Journal of Physics*:

- Conference Series*. 1432:012052. doi: 10.1088/1742-6596/1432/1/012052.
- [19] Thomson, A., Ernst, M., Haedrich, I., & Quian, J. (2017). Impact of PV module configuration on energy yield under realistic conditions. *Optical and Quantum Electronics*, 49, 82. doi: 10.1007/s11082-017-0903-0.
- [20] Shamim, A., Noman, M., Zubair, M., Khan, A.D., & Saher, S. (2018). A facile approach to determine the unknown refractive index (n) and extinction coefficient (k) of novel encapsulant materials used in back contact PV modules. *Applied Physics A*, 124, 542. doi: 10.1007/s00339-018-1974-x.
- [21] Emissivity factor of common materials. Fluke Corporation, <https://www.flukeprocessinstruments.com/en-us/service-and-support/knowledge-center/infrared-technology/emissivity-metals> [accessed: 27 Aug. 2023].
- [22] Guarracino, I., Mellor, A., Ekins-Daukes, N.J., & Markides, C. (2016). Dynamic coupled thermal-and-electrical modelling of sheet-and-tube hybrid photovoltaic/thermal (PVT) collectors. *Applied Thermal Engineering*, 101, 778-795. doi: 10.1016/j.applthermaleng.2016.02.056.
- [23] Hussien, A., Eltayesh, A., & El-Batsh, H.M. (2023). Experimental and numerical investigation for PV cooling by forced convection. *Alexandria Engineering Journal*, 64, 427-440. doi: 10.1016/j.aej.2022.09.006.
- [24] Tepe, A.Ü., Uysal, Ü., Yetişken, Y., & Arslan, K. (2020). Jet impingement cooling on a rib-roughened surface using extended jet holes. *Applied Thermal Engineering*, 178, 115601. doi: 10.1016/j.applthermaleng.2020.115601.
- [25] Ansys Fluent Theory Guide, 2023, <https://www.ansys.com/>
- [26] Pawlucki, M., & Kryś, M. (2020). *CFDs for engineers. Practical exercises on the example of the Ansys Fluent system* (in Polish), Helion SA, Gliwice, pp. 249-256.
- [27] Karava, P., Jubayer, C.M., & Savory, E. (2011). Numerical modelling of forced convective heat transfer from the inclined windward roof of an isolated low-rise building with application to photovoltaic/thermal systems. *Applied Thermal Engineering*, 31, 1950-1963. doi: 10.1016/j.applthermaleng.2011.02.042.
- [28] Lamaamar, I., Tilioua, A., & Hamdi Alaoui, M. A. (2022). Thermal performance analysis of a poly c-Si PV module under semi-arid conditions. *Materials Science for Energy Technologies*, 5, 243-251. doi: 10.1016/j.mset.2022.03.001.